Geophysical Journal International

Geophys. J. Int. (2015) **200,** 777–788
GJI Seismology

doi: 10.1093/gji/ggu433

Modelling infrasound signal generation from two underground explosions at the Source Physics Experiment using the Rayleigh integral

Kyle R. Jones,[1] Rodney W. Whitaker[2] and Stephen J. Arrowsmith[2]

[1] *Ground-Based Monitoring R&E, Sandia National Laboratories, P.O. Box* 5800, *Albuquerque, NM* 87185–0404, *USA. E-mail: krjones@sandia.gov*
[2] *EES*-17 *MSF*665, *Los Alamos National Laboratory, P.O. Box* 1663, *Los Alamos, NM* 87545, *USA*

Accepted 2014 November 5. Received 2014 October 24; in original form 2013 October 28

SUMMARY

We use the Rayleigh integral (RI) as an approximation to the Helmholtz–Kirchoff integral to model infrasound generation and propagation from underground chemical explosions at distances of 250 m out to 5 km as part of the Source Physics Experiment (SPE). Using a sparse network of surface accelerometers installed above ground zero, we are able to accurately create synthetic acoustic waveforms and compare them to the observed data. Although the underground explosive sources were designed to be symmetric, the resulting seismic wave at the surface shows an asymmetric propagation pattern that is stronger to the northeast of the borehole. This asymmetric bias may be attributed to the subsurface geology and faulting of the area and is observed in the acoustic waveforms. We compare observed and modelled results from two of the underground SPE tests with a sensitivity study to evaluate the asymmetry observed in the data. This work shows that it is possible to model infrasound signals from underground explosive sources using the RI and that asymmetries observed in the data can be modelled with this technique.

Key words: Time-series analysis; Controlled source seismology; Seismic monitoring and test-ban treaty verification; Wave propagation; Acoustic properties.

1 INTRODUCTION

The goal of the Source Physics Experiment (SPE) at the Nevada National Security Site (NNSS), is to improve upon and develop new physics-based models for underground nuclear explosion monitoring. An important aspect of this goal is the ability to utilize not only seismic, but infrasound data to further our understanding of underground explosions and event discrimination. Typically, infrasound observations for nuclear explosion monitoring are made at great distances away from a source (Christie & Campus 2010). At these distances the character of the signal has changed dramatically and it can be difficult to derive the near-field characteristics of the source (Szuberla *et al.* 2006). Unlike traditional seismology, the medium through which infrasound waves propagate changes dynamically over very short timescales (Evers *et al.* 2012). Our infrasound deployment for SPE allows us to observe the infrasound generated from the surface ground motion of an underground explosive source at very close range (0.25–5 km), effectively reducing propagation effects such as wind and regional topography.

The challenging aspect of this series of experiments is that they are not simple, above ground sources, but instead are overburied (with respect to traditional underground nuclear testing practice), seismically well-coupled events that interact with the atmosphere in potentially complicated ways due to geology, ground saturation, fracturing from previous explosions, etc. Using data from vertical accelerometers installed azimuthally around ground zero, we use the Rayleigh integral (RI) to produce synthetic infrasound waveforms that can be directly compared to the observed waveforms to explore the effects of surface spall and damage to determine if changes in the source region can be detected and characterized using infrasound.

For an overview of the entire experiment, as well as the shot objectives for past and future tests the reader is referred to the 2013 article in EOS 'Chemical Explosion Experiments to Improve Nuclear Test Monitoring' (Snelson *et al.* 2013). This paper will focus only on the recorded observations from the second and third SPE tests and the efforts to model the source using the RI.

The second explosive test (SPE-2) in the SPE series was conducted on 2011 October 25 at 19:00 UTC. The shot consisted of 997 kg TNT equivalent Sensitized Heavy Ammonium Nitrate and Fuel Oil (SHANFO) buried to a depth of 45.7 m with a scaled depth of burial (SDOB) of 363 m kt^{-3}. The third explosive test (SPE-3) was conducted on 2012 July 24 at 18:00 UTC and consisted of 905 kg TNT equivalent SHANFO at 45.8 m with a SDOB of 376 m kt^{-3}, (Snelson *et al.* 2013). Both explosive shots occurred in the same borehole at ground zero.

1.1 Network of infrasound arrays

The basic experimental set-up was similar for both SPE-2 and SPE-3 in terms of array geometry and sensor locations. For

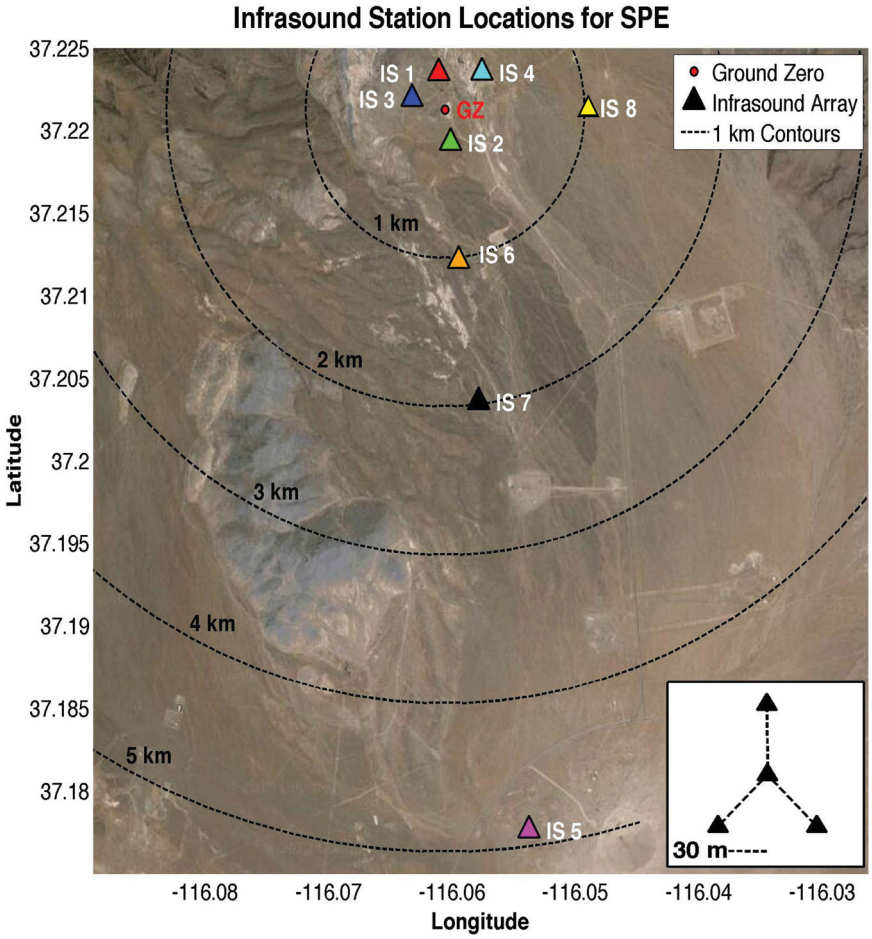

Figure 1. Map showing the eight infrasound array locations (triangles) around ground zero (red) used for SPE-2 and SPE-3. All of the locations were the same for both SPE-2 and SPE-3 with the exception of an additional array (yellow, IS 8) for SPE-3. Dashed lines are radii at 1 km spacing from ground zero for scale. Inset shows the nominal sensor geometry at each array (not to scale).

SPE-2, seven arrays consisting of four Inter-Mountain Labs (IML-ST) infrasound sensors (www.intermountainlabs.com, last accessed 20 November 2014) were deployed around ground zero. The data were recorded using Reftek RT-130 digitizers sampling at 500 sps. The IML-ST sensors have a nominal sensitivity of 0.20 V Pa^{-1} and a flat response from 30 Hz down to where the roll-off begins around 2 Hz (Hart 2007). For this reason, we remove the instrument response from the data prior to processing.

Due to the roll-off of the IML sensors we chose to upgrade to Hyperion IFS-3000's (www.hyperiontg.com, last accessed 20 November 2014) for SPE-3 and all future shots. The IFS-3000 has a flat response from 0.1 to 100 Hz (without porous hoses) and 0.1 to 40 Hz (with porous hoses) with a 100 Pa full scale range and a nominal sensitivity of 0.15 V Pa^{-1}. We recorded the SPE-3 infrasound data on Geotech Instruments SMART-24 digitizers at 200 sps. We lowered the sample rate from 500 to 200 sps for SPE-3 because the majority of the acoustic energy is around 3 Hz and the IFS-3000 response is flat only up to 100 Hz without a correction.

For both SPE-2 and SPE-3 the data were telemetered in real-time to the Sandia trailer at the command centre ∼365 m southeast of ground zero using AFAR 2.4 GHz wireless ethernet bridge radios. The infrasound sensors were installed in a roughly triangular geometry with one sensor and the digitizer at the centre and the other three sensors arranged azimuthally (∼120° increments) around the centre element at a distance of ∼30 m. Attached to each sensor were four lengths of ∼15 m porous hoses for wind noise reduction.

Four arrays were installed azimuthally around the explosives pad approximately 0.25 km from ground zero at different elevations due to topography constraints. For SPE-2 the remaining three arrays were located at 1, 2 and 5 km, respectively linearly south-southeast of ground zero with one additional array installed 1 km east of ground zero for SPE-3 (Fig. 1). The surface acceleration data (discussed in detail in a later section) were recorded using 12 Endevco 500 g vertical accelerometers installed in a 'cross' geometry around ground zero (Fig. 2). Two accelerometers were installed to the north, east and west with the remaining six linearly spaced to the south–southwest. The geometry of the sensors was pre-determined by the space constraints of the explosive pad and surrounding topography.

1.2 Data observations

The ground-motion-generated acoustic wave propagated across the entire network for both SPE-2 and SPE-3 with peak-to-trough amplitudes (1–5 Hz) from ∼13.6 Pa at the closest stations to less than 0.4 Pa at 5 km for SPE-2 and ∼8.4 Pa to less than 0.2 Pa for SPE-3 (Table 1). Waveforms from both tests exhibit a shape that is asymmetric due to phase differences in the source, the off-axis location of the arrays (Fig. 3), and filtering. We will discuss on-axis

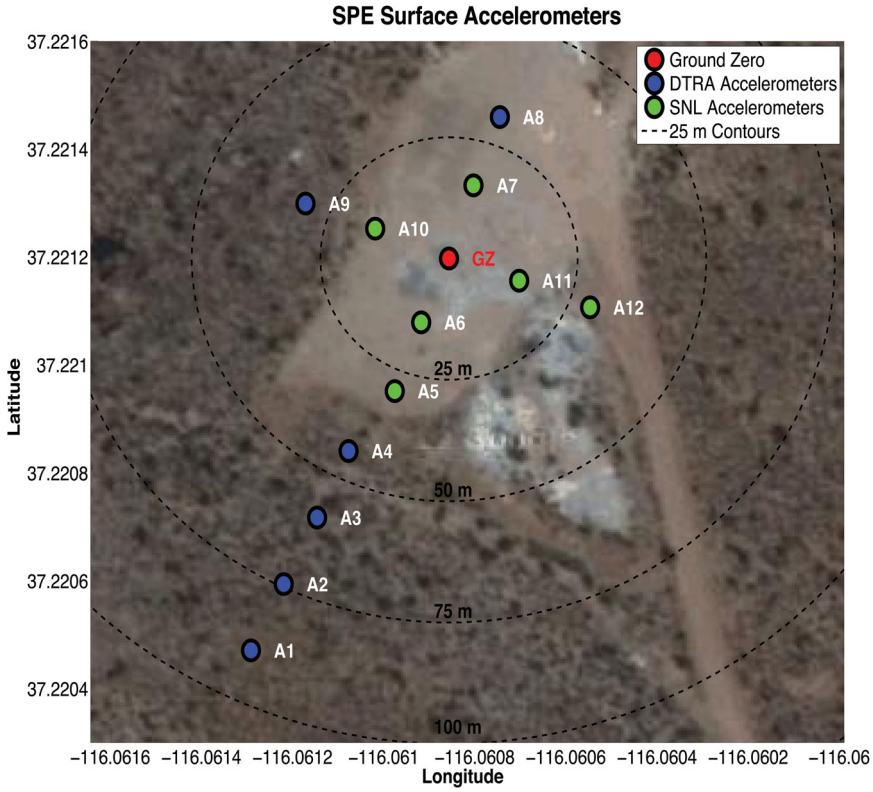

Figure 2. Map of ground zero (red) and surrounding instrument pad showing the locations of 12 Endevco 500 g vertical surface accelerometers installed by Sandia (green) and DTRA (blue). For SPE-3 the Sandia accelerometers were replaced by DTRA accelerometers of the same make and model. This was done so that DTRA recorded all of the accelerometer data. The dashed lines represent distances of 25 m from ground zero.

Table 1. Filtered (1–5 Hz) average peak-to-trough amplitude values for SPE-2 and SPE-3. Station IS 8 was not installed for SPE-2. The measurements were taken from the first initial pulse to the trough.

Array	Avg. distance (km)	Avg. SPE-2 peak-trough (Pa)	Avg. SPE-3 peak-trough (Pa)
IS 1	0.24	10.3	6.4
IS 2	0.25	10.6	7.1
IS 3	0.28	10.9	8.5
IS 4	0.36	9.0	4.6
IS 6	1	3.0	1.7
IS 8	1	–	1.0
IS 7	2	1.3	0.7
IS 5	5	0.4	0.2

versus off-axis pressures and other causes of waveform variability in later sections. Additionally, data from both the surface accelerometers and infrasound sensors show an asymmetric ground motion at the surface above the source hole. This asymmetry is key to the observed waveform shape in the infrasound data and can be traced directly back to the surface ground motion recorded by the accelerometers.

1.3 The RI

The RI allows for the calculation of pressure as a function of time at an arbitrary observation point above an area that has a known acceleration history as a function of time and position. The observation point can be on or off the vertical axis of the ground motion area. Banister (1979), presented an earlier application of the RI to the calculation of near-field, atmospheric pressure signals generated by the surface ground motion from underground nuclear tests. While our work is similar to Banister's, we apply this method to a much smaller source. This method has also been used by Whitaker (2007, 2008, 2009) for modelling infrasound generated from underground nuclear explosions (UGTs) and more recently, the RI has been successfully used to model epicentral infrasound from the M_w 4.7 Circleville earthquake in Utah in 2011 January (Arrowsmith *et al.* 2012). In the Circleville study, the authors calculated the RI on-axis (directly above the source) and then used a directivity function (Bessel function of the second kind) to scale the amplitude according to the appropriate horizontal distance. For our study, we calculate the waveforms and amplitudes based on a horizontal scalar range that corresponds directly to each sensor array and takes into account the amplitude scaling.

Formally, the RI provides a means to calculate the pressure generated by an area of surface acceleration as in eq. (1)

$$p(x, y, z; t) = \rho_0 \int_S \frac{\dot{u}\left(x', y'; t - \frac{R}{C_0}\right)}{2\pi R} \mathrm{d}S, \tag{1}$$

where p is a function of x, y, z and time, ρ_0 is the ambient air density, c_0 is the speed of sound in air, $\dot{u}$ is the surface acceleration, x', y' are the coordinates of each source point on the area dS of the surface and R is the distance from the point x', y' to the observation point (Blackstock 2000). Fig. 4 shows the geometry used in the RI.

For the application of the RI to the calculation of near-field infrasound signals, from underground explosions, the source of the surface ground motion is the upward propagating stress/elastic wave

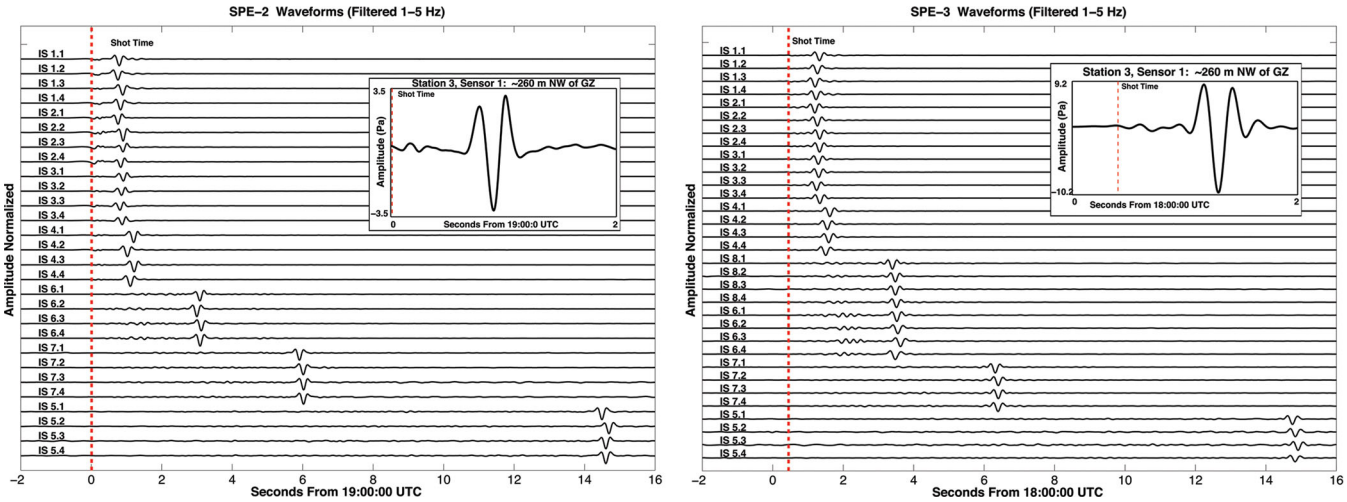

Figure 3. Waveforms from SPE-2 (left-hand side) and SPE-3 (right-hand side) for each sensor arranged according to distance and band pass filtered between 1 and 5 Hz. The explosion propagated across the entire network out to 5 km. The Inset shows an example waveform from station 3, sensor 1.

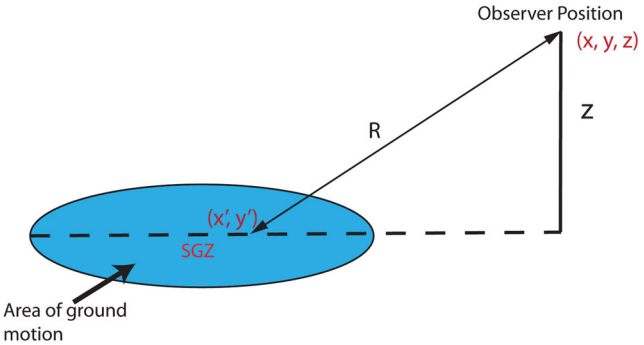

Figure 4. Illustration of the observer parameters in the Rayleigh integral technique. SGZ is the surface ground zero at the centre of the ground motion. The observer is at a slant distance *R* from SGZ.

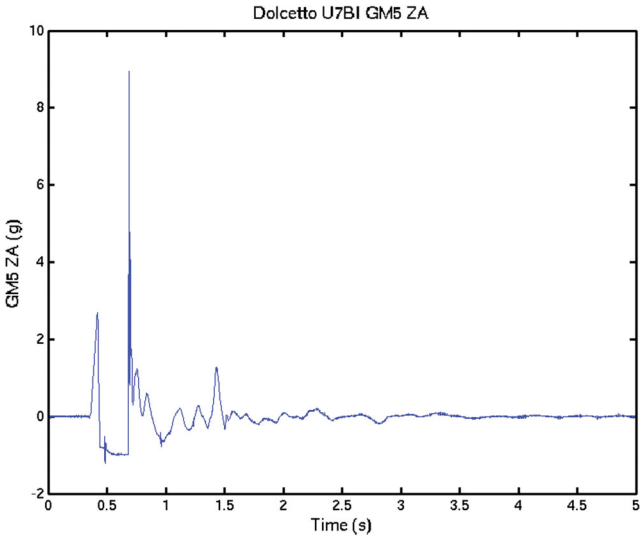

Figure 5. Measured vertical ground motion acceleration record from underground nuclear test Dolcetto at the Nevada Test Site on 1984 August 30. The plot shows the acceleration time history where amplitude is in *g*. The −1 g spall phase is seen in the acceleration record near 0.5 s.

from the explosion. Acceleration amplitudes are generally largest at surface ground zero and decay radially outward with distance. When the elastic wave reaches the surface, the vertical ground motion drives a signal in the atmosphere. This can be visualized as a piston mounted in an infinite, rigid baffle, where the piston, in reality, is not completely rigid.

In some cases, the ground may be driven into tensile failure, known as spall, and is recorded as a −1 g acceleration after the initial elastic upward pulse. Spall was commonly observed for underground nuclear tests. For illustration, Fig. 5, shows an example of spall from underground nuclear test Dolcetto at the Nevada Test Site on 1984 August 30.

The acceleration records for SPE-2 (Fig. 6) and SPE-3 (Fig. 7) show spall similar to that seen in previously recorded underground nuclear explosions. While vertical ground motion without spall can generate an atmospheric signal, as demonstrated by earthquake-generated infrasound, spall is an important contributor to the near-field infrasound signal. In the simple parabola model for the surface acceleration, the peak velocity determines the ground motion after the initial acceleration pulse (Lee & Walker 1980).

1.4 Vertical surface accelerations as a source

To model the source we use a 200 m^2 grid (for simplicity) with ground zero at the center. The Defense Threat Reduction Agency (DTRA) and Sandia National Labs (SNL) both used the same brand of accelerometer (ENDEVCO 500 g) to record the surface accelerations for SPE-2. DTRA sampled at a rate of 1 000 000 sps and SNL used 4000 sps. The DTRA data were down-sampled by a factor of 1000 and the SNL data by a factor of 4 so that both data sets matched at 1000 SPS for use in our analysis. For SPE-3 the SNL accelerometers were replaced with the DTRA ENDEVCO 500 g sensors and recorded directly on a DTRA digitizer (Fig. 8). This was done to ensure consistency in the surface accelerometer data.

As applied to SPE-2 and SPE-3, the RI uses the unfiltered, vertical accelerations recorded at the 12 surface accelerometers located at surface ground zero. The area is divided into uniform square elements, d*S*, to form a grid encompassing the area of uplift. It should be noted that the lateral extent during peak acceleration is closer to 120 m × 120 m and not the entire 200 m × 200 m area of the grid. The acceleration in each elemental area (d*S*) was defined by interpolating and extrapolating the accelerations observed by the 12 accelerometers for each sample in time from 0 to 0.4 s over the entire grid area. To do this, we needed to find a way to both interpolate and

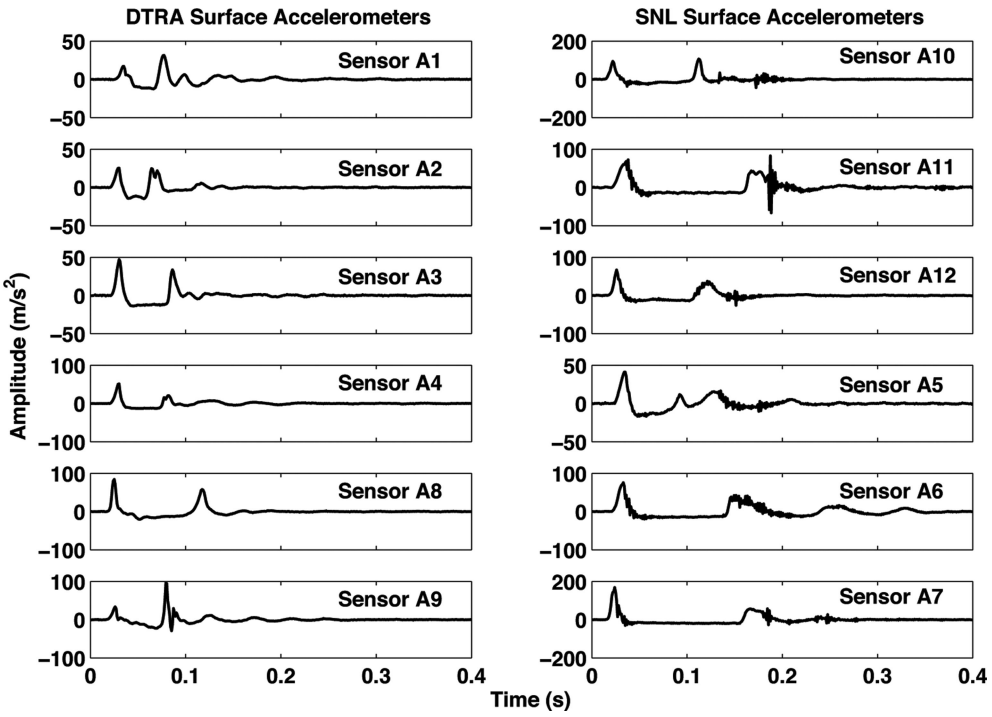

Figure 6. SPE-2 DTRA and SNL surface accelerometer records (unfiltered) out to 0.4 s. See Fig. 2 for sensor locations. Spalling is evident in most of the records.

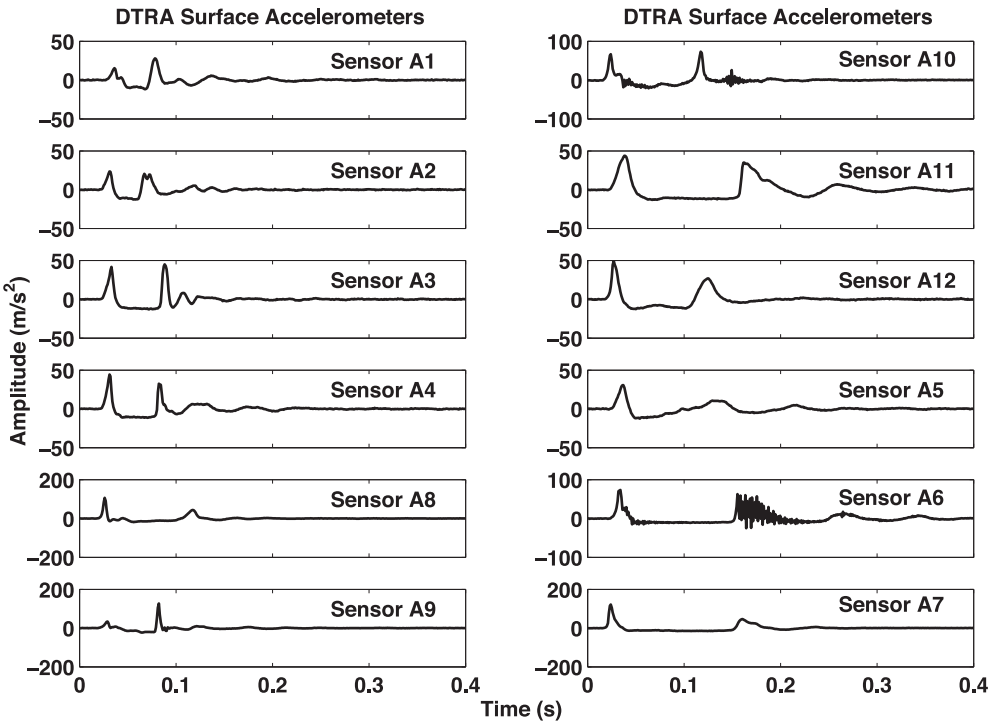

Figure 7. SPE-3 DTRA surface accelerometer records (unfiltered) out to 0.4 s. See Fig. 2 for sensor locations.

extrapolate the grid using only 12 sparse data points. Attempting to use the built-in Matlab© functions for linear, cubic spline and quadratic interpolation/extrapolation resulted in artefacts that were 'non-physical' and caused the synthetic infrasound waveform to be unrealistic. Specifically, the synthetic waveform was dominated by a very low frequency component not observed in the actual data. Further investigation found that this was due to a 'rocking' or 'tilting' of the grid during the extrapolation process. We solved these issues by using radial base functions (RBF) as described by Morse *et al.* (2005) and using code developed by Alex Chiokov (2006) to interpolate over a non-uniform, sparse data set (Fig. 8).

We also 'pinned' the edges of the grid to zero to simulate the edges of the surface source region, which, in reality, are not detached from the surrounding area. We felt that this was an appropriate measure to

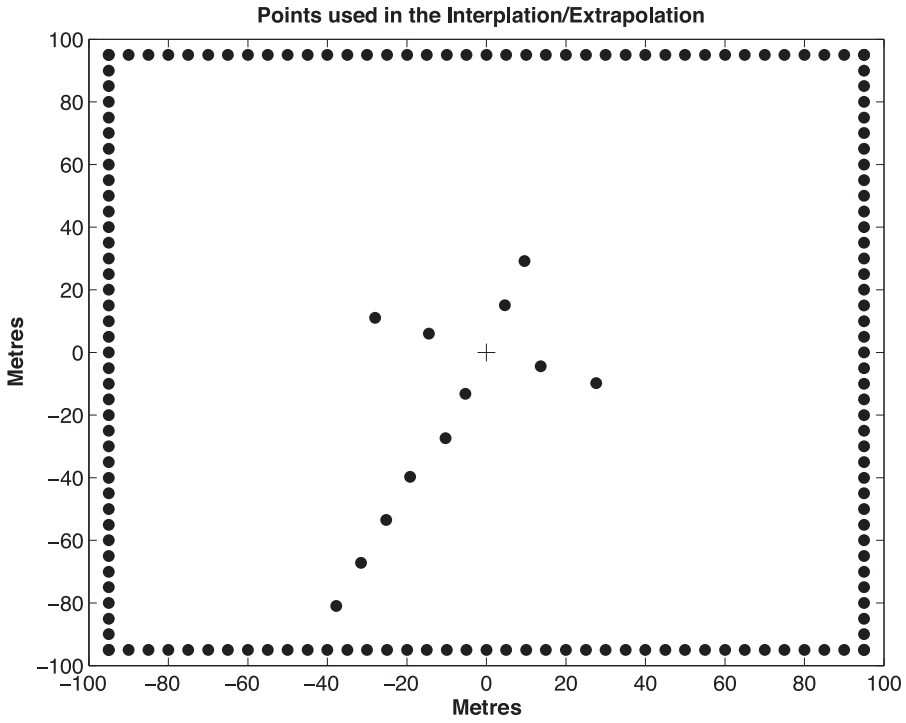

Figure 8. Points used in the interpolation/extrapolation process, including the accelerometers (cross) around ground zero (+) and the fixed points (surrounding box) that were used to reduce the extrapolation artefacts. The interpolation/extrapolation was done using radial base functions, which support a non-uniform, scattered data set.

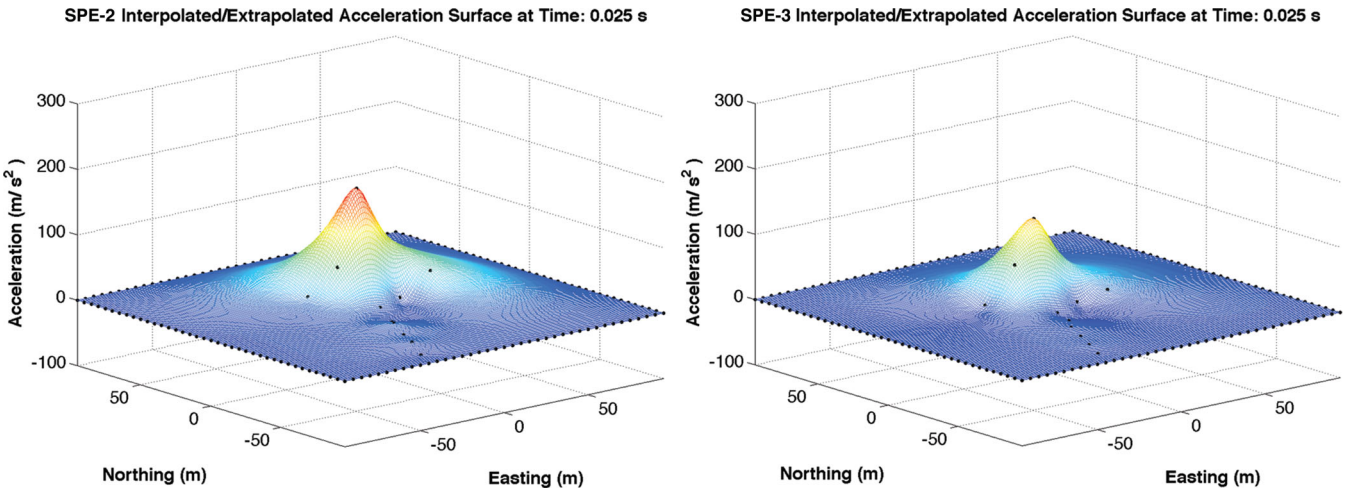

Figure 9. Interpolated and extrapolated acceleration surface for SPE-2 (left-hand side) and SPE-3 (right-hand side) showing the peak acceleration at time 0.025 s after detonation. Note that the area of maximum acceleration is not centred on the ground zero (0,0), resulting in an asymmetric source.

ensure a more realistic result. As an example, Fig. 9 shows the entire extrapolated grid for SPE-2 (left-hand side) and SPE-3 (right-hand side) at time 0.025 s after detonation, corresponding to the peak acceleration. In this case the maximum-recorded acceleration does not occur exactly above ground zero, resulting in an asymmetric surface acceleration.

1.5 The RI and constraining the Rayleigh distance

Before we discuss the results of this work we thought it important to have a brief discussion on the importance of the Rayleigh distance in regards to our model and assumptions. The Rayleigh distance (R_0), as defined by Blackstock (2000), is the distance at which an acoustic signal transitions from a 'near-field' propagation regime to the standard 'far-field' propagation regime, and is given in eq. (2)

$$R_0 \equiv \frac{S}{\lambda}, \tag{2}$$

where S is the area of the baffle and λ is the wavelength of the acoustic signal. For this study, we initially compared the observed and synthetic signals between 1 and 10 Hz. If we use the entire 200 m × 200 m grid to find R_0 for signals in our frequency range we find that for a sound speed of 344 m s^{-1}, R_0 at 1 Hz is 116.3 m, while at 10 Hz it becomes 1163 m. At the high end of the frequency band, and for energy above 2.2 Hz, R_0 is greater than the

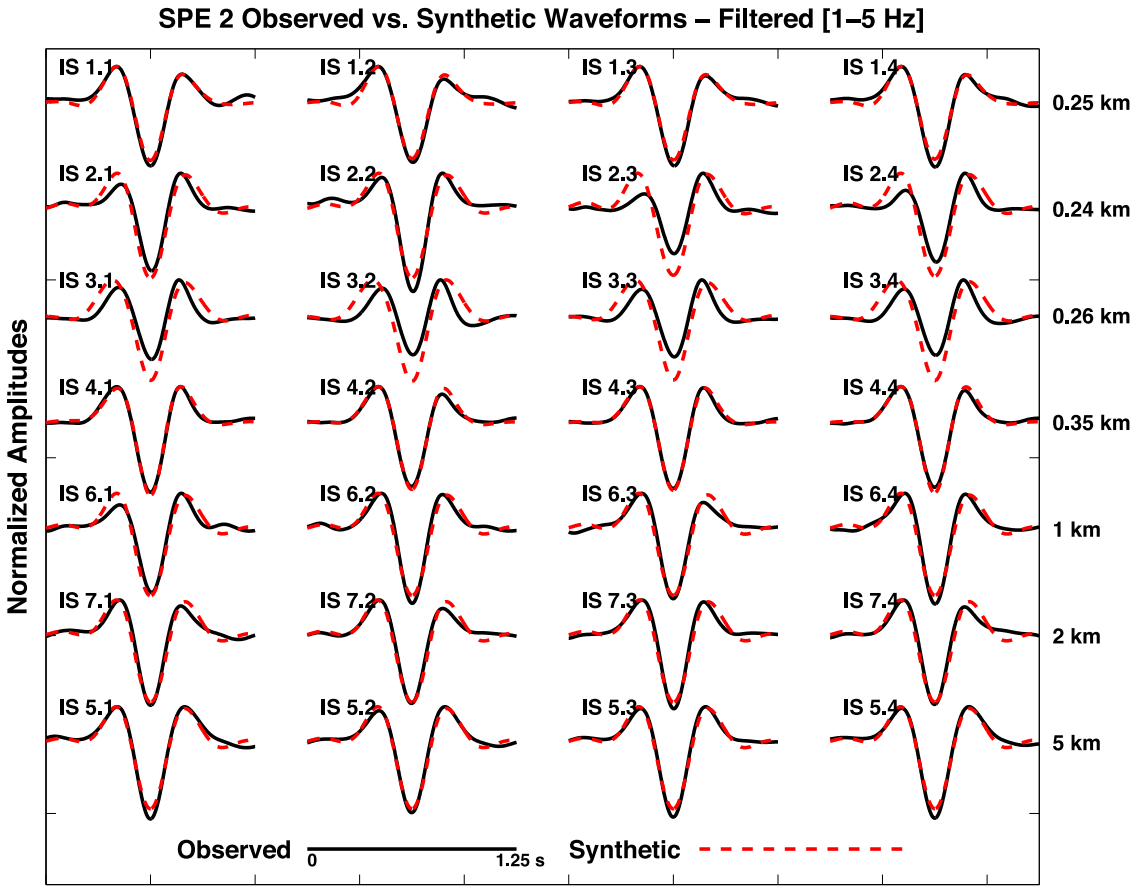

Figure 10. SPE-2 synthetic pressure traces produced by the Rayleigh integral (dashed red line) compared to the observed data (solid black line) shown for all sensors in the array network. Overall, the waveform shape is reproduced very well with slight variability at arrays 2 and 3. *Note:* 'IS N.M' represents infrasound array N station M.

closest infrasound array. However, in the frequency domain the peak acoustic energy for the explosion occurs at 3 Hz and during peak acceleration, the maximum area of uplift is roughly 120 m × 120 m. Considering these two parameters, R_0 for 1 and 10 Hz becomes 41.9 and 419 m, respectively. In this case the energy above 6 Hz has a Rayleigh distance beyond our closest array. Since the majority of the acoustic energy is around 3 Hz and only a small portion is above 6 Hz, we felt that it was appropriate to use the RI to produce synthetic waveforms that were band limited between 1 and 5 Hz so that the calculations and comparisons were sufficiently in the 'far-field'.

1.6 Comparing observed and synthetic waveforms for SPE-2

Using the RI to generate synthetic waveforms, we compared each station's observed data to a set of synthetic waveforms corresponding to the same distances. We found that, to first order, the synthetic waveforms correlated well, when normalized, with the observed data for overall waveform shape. This did not hold true for each and every station comparison. For example, the 5 km station showed a phase shift where the synthetic trace shows an arrival before the observed arrival. The time delay could be attributed to topography or wind, which the model does not account for. At the distance of 5 km, topography would have a minimal effect on the traveltime such that the difference can, most likely, be attributed to wind. At the time of the test there was a 6 m s^{-1} wind from the south acting directly against the southward propagation of the pressure wave, resulting in a time delay of ∼0.25 s. For simplicity and for later data comparison, we use cross-correlation to align the synthetic waveform with the corresponding observed waveform. For this study the phase shifts and absolute amplitudes are less important than overall waveform shape because without wind data at each array and *in situ* calibration of the porous hoses we have no way quantify the variability. All of the waveform comparisons for SPE-2 are shown in Fig. 10.

Overall, the shape of the normalized synthetic waveforms fit the observed data very well. In particular, arrays 1, 4, 6, 7 and 5 visually show a high degree of correlation in shape and in all cases, the period matches well. The variability seems to occur primarily in the side lobes and in the main trough and could be related to a number of circumstances that our simplistic model does not account for. The RI is primarily intended for far-field calculations well above the source. We are testing the limits of this method by calculating waveforms at close range with little to no vertical relief. However, with the results shown above, the RI accurately reproduces the observed waveforms. Additionally, there could be 'microscale' topography variability, unaccounted for by our method, in which, the sensors at each array are not planar relative to one another. For example, for the close-in arrays, there was limited room for the spatial extent of the installation causing several of the sensors to be installed behind a small rise or significantly lower/higher than the rest of the array. Another potential source of variability can be attributed to the porous hose wind filter system installed on each sensor. The porous hoses are left out for multiple deployments and it is unknown to

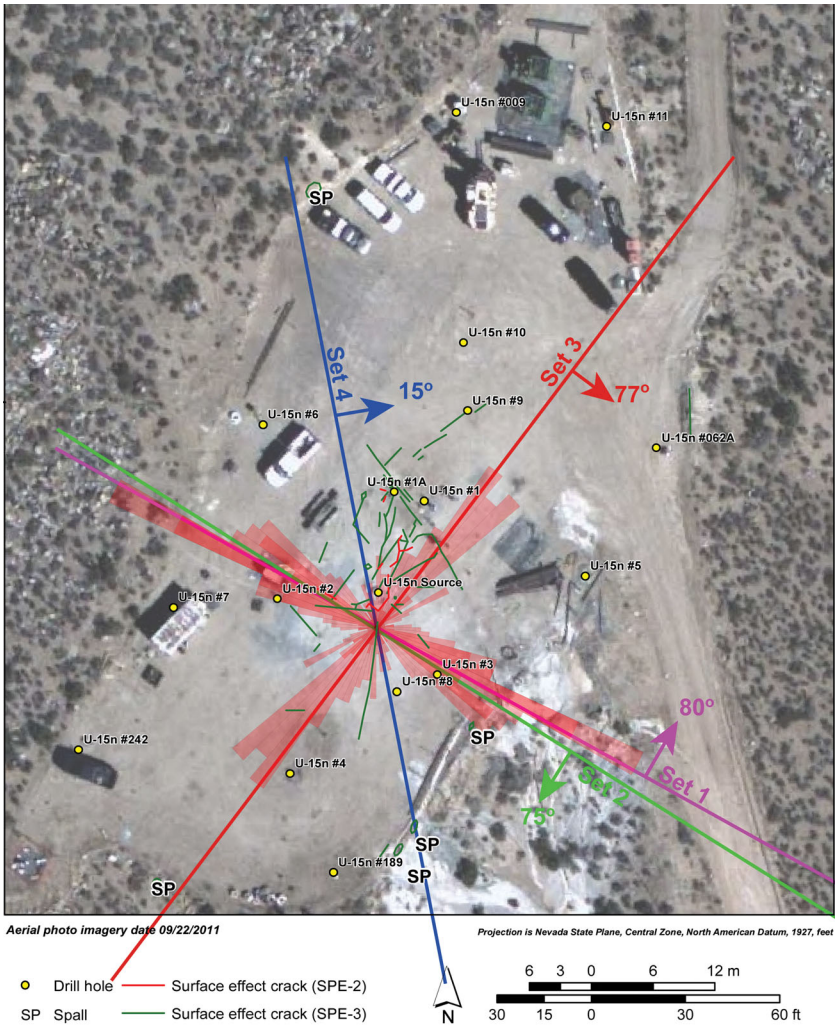

Figure 11. Aerial photo of the SPE Pad showing mapped fractures for SPE-2 (red) and SPE-3 (dark green) (Drellack *et al.* 2012). The majority of the fractures exist to the Northeast of the emplacement hole in the same area as the maximum acceleration as shown in Fig. 9.

what degree the elements (sun, rain, dust, etc.) have on the recorded signal. A future study is planned to determine if the porous hoses show significant variability with aging.

1.7 Observed asymmetry and symmetric modelling of the source region for SPE-2

While plotting the acceleration surfaces, we noticed that the area of uplift due to the explosion is not uniform around surface ground zero. We believe this could be due to one or more types of variations in site characteristics. One factor could be differential offset along natural fracture sets present throughout the granite body. Specifically, after each test, fracture mapping was conducted at the surface. Fig. 11 shows mapped fractures after SPE-2 (red) and SPE-3 (green) that correlate well with the location of peak acceleration for both tests. Another possible contributing factor could be variations in the fill material that had been placed on the native granite surface to create a level construction pad; this fill varies in thickness across the pad, generally thickening to the southeast. These or other site factors could contribute to a differential response in different portions of the construction pad. The resulting pressures waves from the explosion reacted differently across the pad and excited the surface non-uniformly (Drellack *et al.* 2011, 2012).

In an attempt to verify that the asymmetry was real and not an artefact of the interpolation/extrapolation process we ran simulations using an azimuthally symmetric synthetic source, generated by taking the southwest accelerometer line and rotating it every 10° around ground zero (Fig. 12). After the new acceleration grid was created, we again interpolated/extrapolated and produced synthetic waveforms for each station in the array. Comparisons between the azimuthally symmetric synthetic waveforms and the observed SPE-2 data for the same set of stations are shown in Fig. 13. While comparing the azimuthally symmetric synthetic waveforms to the observed data, some differences are apparent. Overall, the period of the synthetics visually correlate well to the observed waveforms. However, because the synthetic is symmetric, the waveforms do not achieve the same asymmetric match in the side-lobes that the original synthetics show, leading to over- or underestimated peak amplitudes in most cases. Similar to the asymmetric case, the trough of the waveform is also overestimated at arrays 2 and 3.

1.8 SPE-2 asymmetric—symmetric error analysis

To more rigorously summarize and compare the differences in fit between the synthetic and azimuthally symmetric synthetic waveforms we calculated the normalized rms error for each

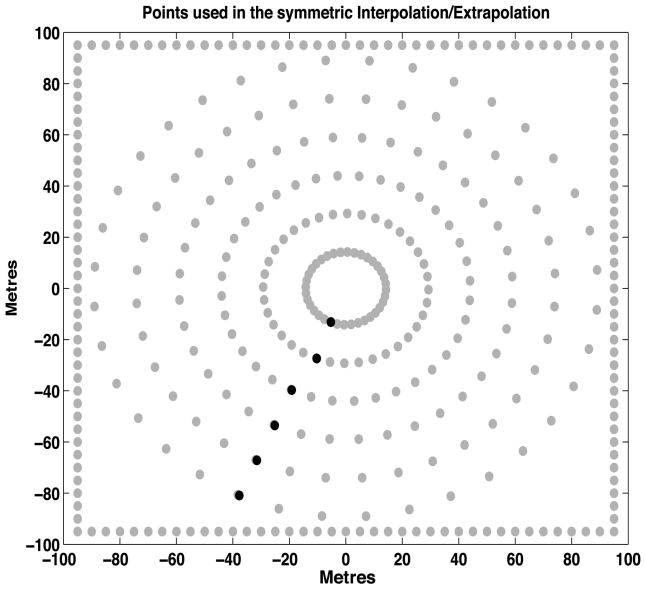

Figure 12. Points used in the azimuthally symmetric interpolation/extrapolation. The black dots are the original accelerometers along the Southwest line and the grey dots are the rotated Southwest line used in the simulation.

synthetic waveform as compared to the observed SPE-2 data (Fig. 14). This was done by first normalizing each and synthetic waveform, individually, by dividing by the data norm and then computing the rms error between each pair. The rms error is notably higher for the azimuthally symmetric synthetic comparisons at all arrays when directly compared to their asymmetric array counterpart. This corroborates what can be seen visually when comparing both synthetic data sets to the observed data.

1.9 Comparing observed and synthetic waveforms for SPE-3

Satisfied that the correct input to the RI is from the recorded, asymmetric accelerometer traces, we re-computed the synthetics using the accelerations recorded for SPE-3 (Fig. 7). Both the accelerations and resulting synthetic waveforms are remarkably similar to the SPE-2 results. For SPE-3, the synthetic waveforms appear to match the observed data better than the synthetics calculated for SPE-2. This could be due to several factors such as reduced wind noise during the time of the shot or that a different sensor with better frequency response was used.

1.10 Comparing SPE-2 and SPE-3 synthetic waveforms

In an effort to understand the differences between the synthetics for SPE-2 and SPE-3 we plotted them together for all arrays (Fig. 16). Note that array IS 8 was added for SPE-3 and thus has no SPE-2 counterpart. The normalized synthetics calculated for both SPE-2 and SPE-3 overlay very well. This could mean that the accelerations from both tests are similar such that they produce extremely similar synthetic waveforms in shape. However, we see slightly larger differences when comparing the synthetic waveforms and the observed

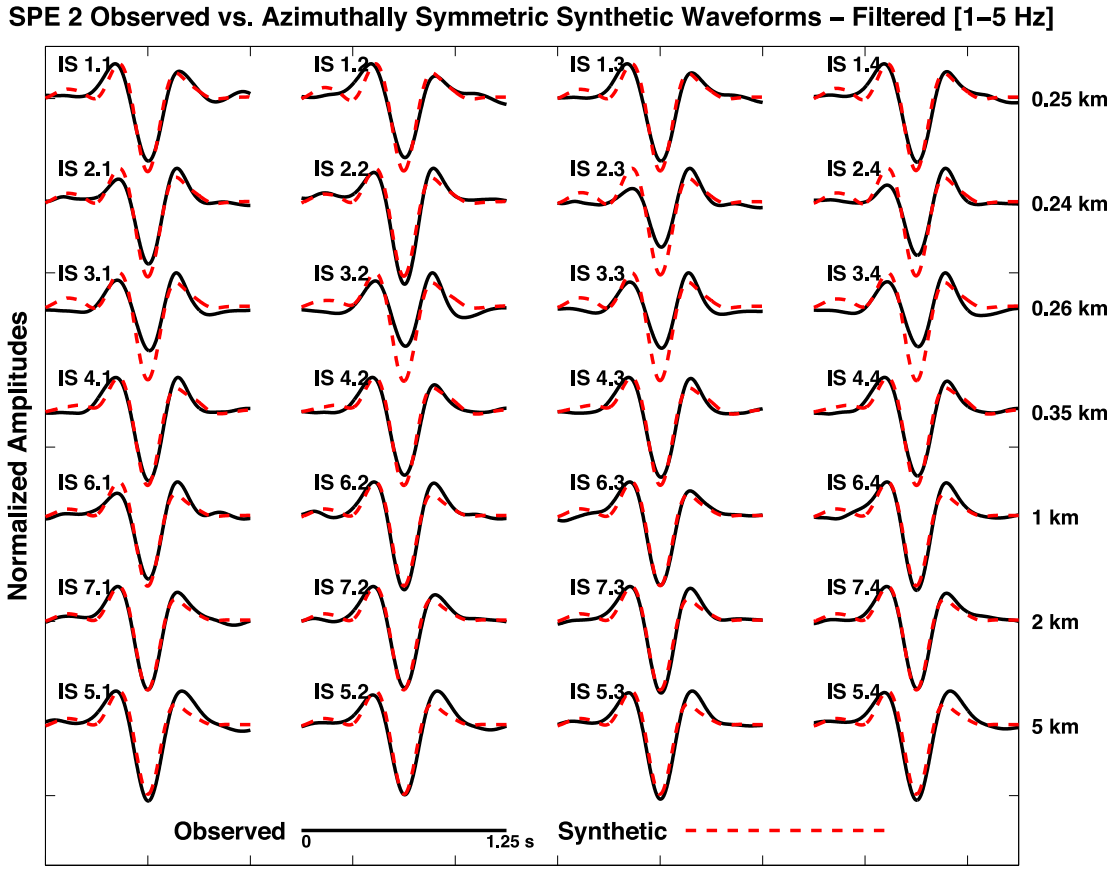

Figure 13. Synthetic pressure traces produced by the Rayleigh integral (dashed red line) using an azimuthally symmetric synthetic source compared to the observed data (solid black lines) for all sensors in the array network.

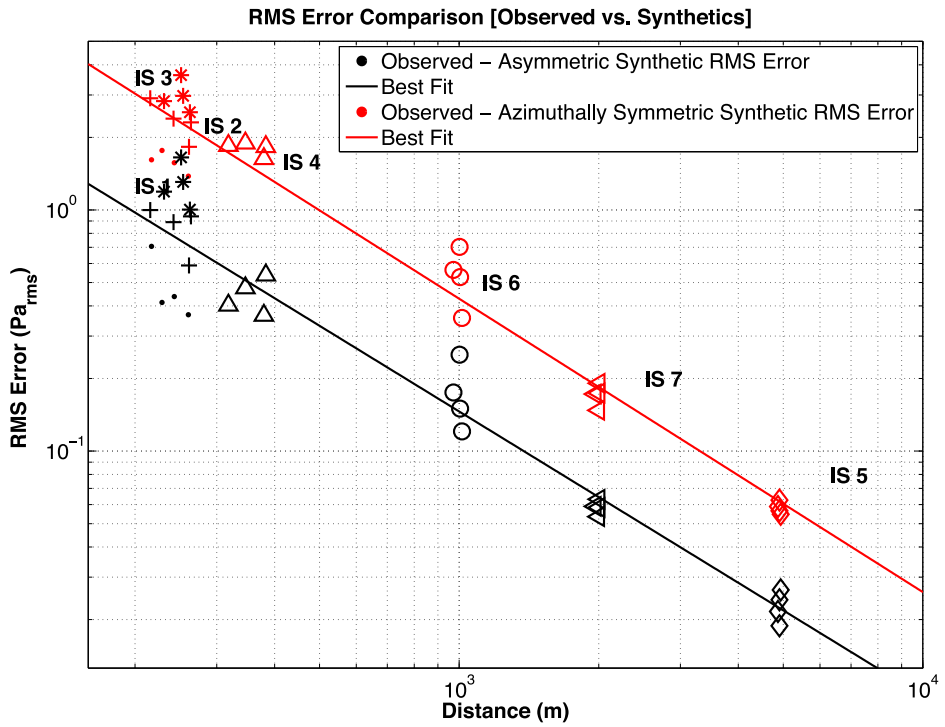

Figure 14. The rms error comparison between the SPE-2 observed waveforms and the asymmetric synthetic waveforms (black) and the observed waveforms and the azimuthally symmetric synthetic waveforms (red). Trend lines are fit to each comparison set.

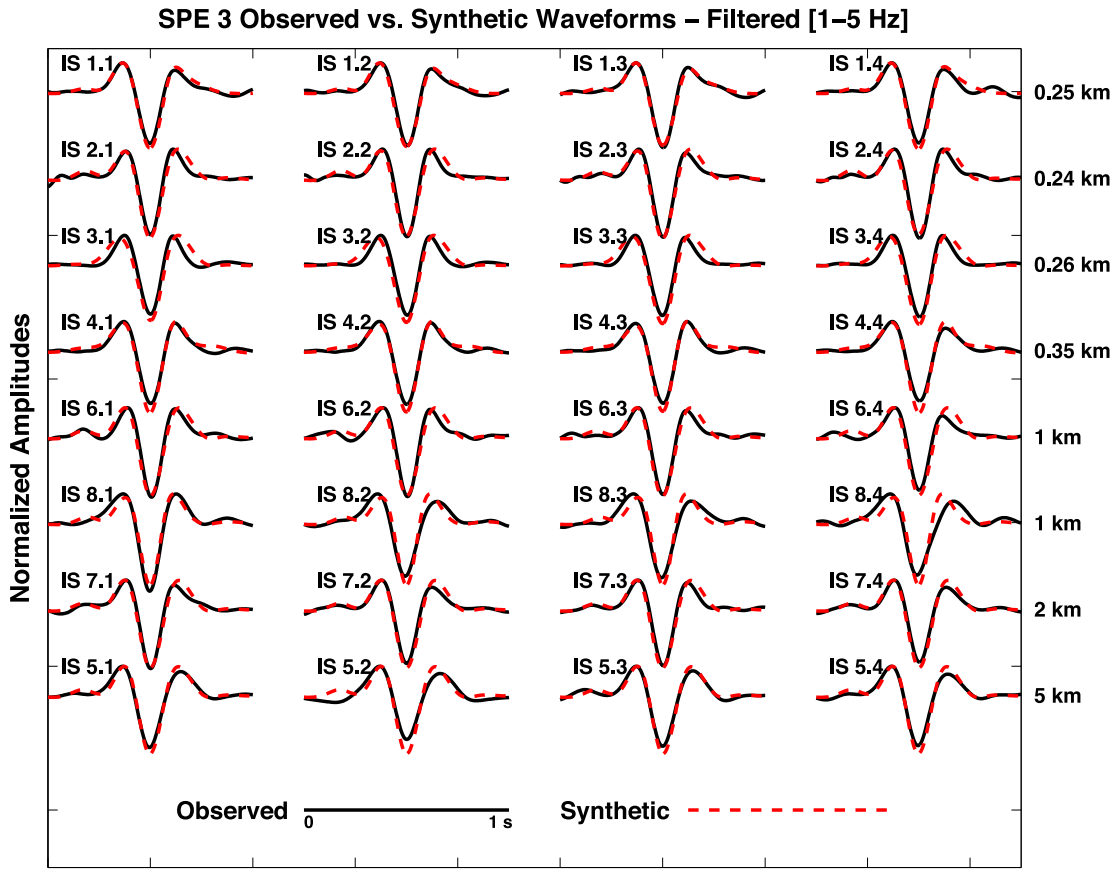

Figure 15. SPE-3 synthetic pressure traces produced by the Rayleigh integral (dashed red line) compared to the observed data (solid black line) shown for all sensors in the array network. The synthetic waveforms appear to be a better fit than the synthetic waveforms calculated for SPE-2. *Note:* 'IS N.M' represents infrasound array N station M.

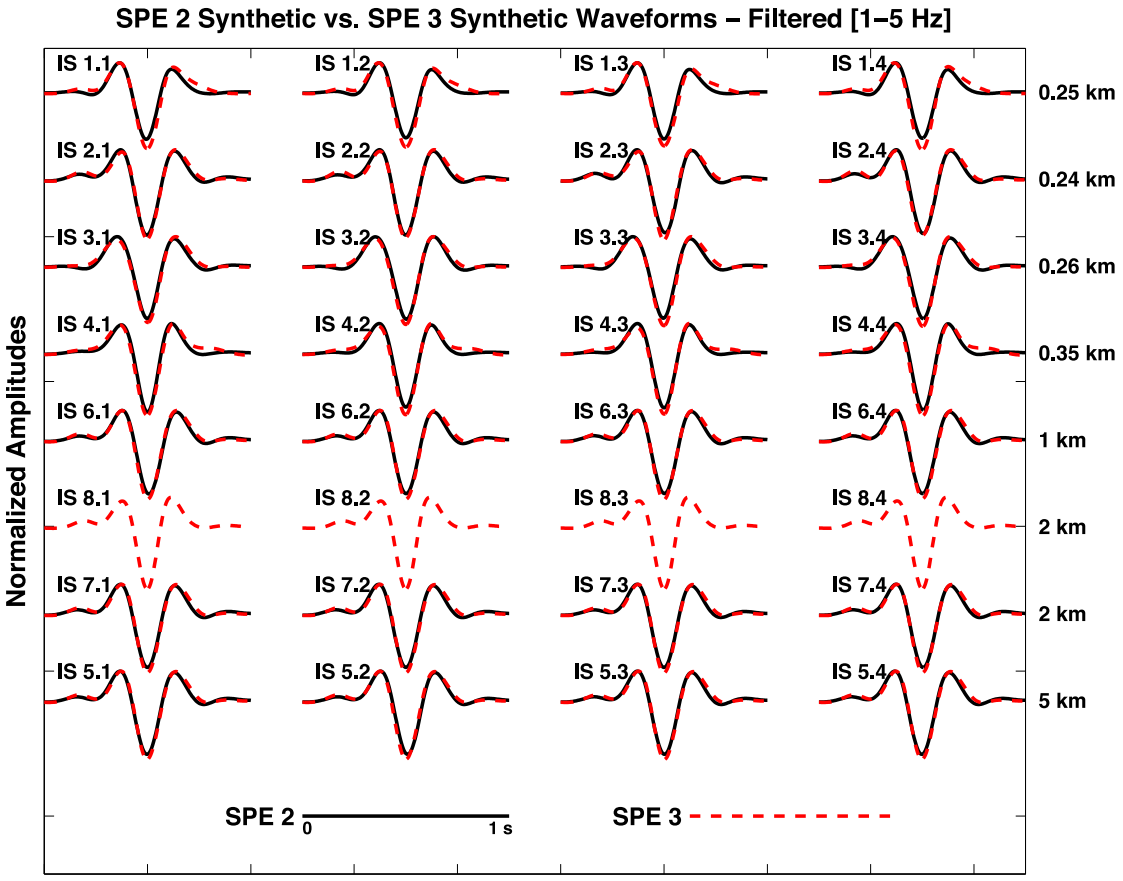

Figure 16. SPE-2 (solid black line) and SPE-3 (dashed red line) synthetic pressure traces produced by the Rayleigh integral for all sensors in the array network. One additional station (IS-8) was installed for SPE-3 and is shown only for completeness. *Note:* 'IS N.M' represents infrasound array N station M.

waveforms than when comparing just the synthetics to themselves. More work is needed to fully understand these differences.

2 DISCUSSION AND CONCLUSIONS

The repetitive nature of the SPE test series provides an excellent opportunity to study infrasound generation from underground explosive tests in a controlled and highly instrumented environment. The 'close-in' deployment of infrasound arrays and other multidisciplinary technologies, such as surface accelerometers, enables detailed modelling of the source region. Specifically, how variations in the geology between the explosive source and the free surface lead to an asymmetric acoustic source that can be detected with a network of infrasound arrays.

We demonstrate that the RI can be used to produce synthetic pressure waveforms from a large distributed source region using a sparse network of surface accelerometers as an input source. We have shown that overall shape and asymmetry of the resulting synthetic waveforms is similar to the observed waveforms, after normalization, for both SPE-2 and SPE-3. For SPE-2, an error analysis study between the asymmetric and azimuthally symmetric sources suggests that there is a portion of the source that is not being reproduced accurately azimuthally around ground zero. The relative rms error between the symmetric and asymmetric models showed that rotating one line of accelerometers around ground zero came close to reproducing the observed data but resulted in higher error. In addition, it is possible that the asymmetric model does not represent the true extent of the ground motion and there may be other, non-vertical, components of the ground motion that couple to the atmosphere to produce the observed waveforms in such a way that neither the azimuthally symmetric model nor the original model accurately capture all of the physics involved. Furthermore, both the infrasound array geometry and the surface accelerometer locations are not optimal to completely define and capture the extent of the ground-to-air coupling. All but two of the infrasound arrays are below the elevation of the ground zero and the four closest arrays are within the Rayleigh distance above 6 Hz. The surface accelerometer placements are sparse, making the reconstruction of the source non-trivial. However, after taking into account all of the above caveats, we conclude that it is possible to accurately model the surface-to-air coupling of ground motion into the atmosphere from underground explosions using a sparse network of accelerometers and infrasound sensors using the RI technique.

Future work will include data from future SPE tests as well as models that are based on a completely synthetic source term in addition to surface accelerometer data. We will be looking into amplitude specific variations to evaluate and estimate damage from previous tests. We also plan to use a time-domain, finite-difference, computational fluid dynamics code to compute the evolution of the infrasound signal in the atmospheric domain. Additionally, both the infrasound array network and surface accelerometers will be reconfigured and installed to better capture the subtle variations of the source in phase two of the SPE series of tests.

ACKNOWLEDGEMENTS

The authors want to thank Bobby Corbell (Sandia – Ret.) for deploying and collecting the SPE-2 data set as well Bob White and Ryan Emmitt (NSTec) for their invaluable and continued field efforts in support of this project. We would also like to thank Maggie Townsend (NSTec) for her valuable insight into the geology and surface fracturing of the SPE source region and Artie Rodgers (LLNL) for his insightful comments and feedback on the analysis. The SPEs would not have been possible without the support of many people from several organizations. The authors wish to express their gratitude to the National Nuclear Security Administration, Defense Nuclear Nonproliferation Research and Development (DNN R&D), and the SPE working group, a multi-institutional and interdisciplinary group of scientists and engineers. This work was done by Sandia National Laboratories and Los Alamos National Laboratory under award number DE-AC52-06NA25946. Sandia National Laboratories is a multi-program laboratory managed and operated by Sandia Corporation, a wholly owned subsidiary of Lockheed Martin Corporation, for the U.S. Department of Energy's National Nuclear Security Administration under contract DE-AC04-94AL85000. SAND2013-9173J. Los Alamos National Laboratory is operated by Los Alamos National Security, LLC, for the U.S. Department of Energy's NNSA.

REFERENCES

Arrowsmith, S.J., Burlacu, R., Pankow, K., Stump, B., Stead, R., Whitaker, R. & Hayward, C., 2012. A seismoacoustic study of the 2011 January 3 Circleville earthquake, *Geophys. J. Int.,* **189,** 1148–1158.

Banister, J.R., 1979. A program for predicting ground motion induced air pressures, SAND 78-2361, Sandia National Laboratories, Albuquerque, NM.

Blackstock, D.T., 2000. *Fundamentals of Physical Acoustics,* John Wiley and Sons, 541 pp.

Chiokov, A., 2006. Scattered data interpolation and approximation using radial base functions, Available at: http://www.mathworks.com/matlabcentral/fileexchange/10056, last accessed 20 November 2014.

Christie, D.R. & Campus, P., 2010. The IMS infrasound network: design and establishment of infrasound stations, in *Infrasound Monitoring for Atmospheric Studies,* pp. 29–76, eds Le Pichon, A., Blanc, E. & Hauchecorne, A., Springer.

Drellack, S.L., Prothro, L.B. & Reed, D.N., 2011. Written communication. Subject: "Source Physics Experiment 2 Test Crack Mapping", National Security Technologies, LLC, Las Vegas, NV.

Drellack, S.L., Gonzales, J.L. & Prothro, L.B., 2012. Written communication. Subject: "Geologic Surface Effects Mapped Following Source Physics Experiment 3", National Security Technologies, LLC, Las Vegas, NV.

Evers, L.G., Van Geyt, A., Smets, P. & Fricke, J., 2012. Anomalous infrasound propagation in a hot stratosphere and the existence of extremely small shadow zones, *J. geophys. Res.,* **117,** doi:10.1029/2011JD017014.

Hart, D.M., 2007. Evaluation of Inter-Mountain Labs Infrasound Sensors July 2007, Sandia National Labs Technical Report, SAND2007-7020, Albuquerque, NM.

Lee, H. & Walker, J.J., 1980. Model for ground motion and atmospheric overpressure due to underground nuclear explosions, Los Alamos Scientific Laboratory Report. LA-8554-MS.

Morse, B.S., Yoo, T.S., Rheingans, P., Chen, D.T. & Subramanian, K.R., 2005. Interpolating implicit surfaces from scattered surface data using compactly supported radial basis functions, in *Proceedings of the ACM SIGGRAPH courses, ACM, 2005*, pp. 78–87.

Snelson & Catherine, M. *et al.*, 2013. Chemical explosion experiments to improve nuclear test monitoring, *EOS, Trans. Am. geophys. Un.,* **94**(27), 237.

Szuberla, C.A.L., Arnoult, K.M. & Olson, J.V., 2006. Discrimination of near-field infrasound sources based on time-difference of arrival information, *J. acoust. Soc. Am.,* **120,** EL20–EL28.

Whitaker, R., 2007. Infrasound signals as basis for event discriminants, in *Proceedings of the 29th Monitoring Research Review: Ground-Based Nuclear Explosion Monitoring Technologies,* LA-UR-07-5613, Vol. 1, pp. 905–913, Available at: http://www.osti.gov/bridge/product.biblio.jsp?osti_id=1027449, last accessed 20 November 2014.

Whitaker, R., 2008. Infrasound signals from ground motion sources, in *Proceedings of the 30th Monitoring Research Review: Ground-Based Nuclear Explosion Monitoring Technologies,* LA-UR-08-05261, pp. 912–920, Available at: http://www.osti.gov/bridge/product.biblio.jsp?osti_id=960561, last accessed 20 November 2014.

Whitaker, R., 2009. Infrasound signals from ground motion sources, in *Proceedings of the 30th Monitoring Research Review: Ground-Based Nuclear Explosion Monitoring,* LA-UR-09-05276, pp. 750–758, Available at: http://www.osti.gov/bridge/product.biblio.jsp?osti_id=992203, last accessed 20 November 2014.